

Measurement of high- Q^2 charged current cross sections in e^+p deep inelastic scattering at HERA

ZEUS Collaboration

Abstract

Cross sections for e^+p charged current deep inelastic scattering at a centre-of-mass energy of 318 GeV have been determined with an integrated luminosity of 60.9 pb^{-1} collected with the ZEUS detector at HERA. The differential cross-sections $d\sigma/dQ^2$, $d\sigma/dx$ and $d\sigma/dy$ for $Q^2 > 200 \text{ GeV}^2$ are presented. In addition, $d^2\sigma/dxdQ^2$ has been measured in the kinematic range $280 \text{ GeV}^2 < Q^2 < 17000 \text{ GeV}^2$ and $0.008 < x < 0.42$. The chiral structure of the Standard Model is investigated in terms of the $(1-y)^2$ dependence of the double-differential cross section. The predictions of the Standard Model agree well with the measured cross sections. The mass of the W boson propagator is determined to be $M_W = 78.9 \pm 2.0 \text{ (stat.)} \pm 1.8 \text{ (syst.)}^{+2.0}_{-1.8} \text{ (PDF) GeV}$ from a fit to $d\sigma/dQ^2$. The structure-function F_2^{CC} has been extracted by combining the measurements presented here with previous ZEUS results from e^-p scattering extending the measurement obtained in a neutrino-nucleus scattering experiment to a significantly higher Q^2 region.

1 Introduction

Measurements of deep inelastic scattering (DIS) of leptons on nuclei have been vital in the development of our understanding of the structure of nucleons. In the Standard Model (SM), charged current (CC) DIS is mediated by the exchange of the W boson. In contrast to neutral current (NC) interactions, where all quark and antiquark flavours participate, only down-type quarks and up-type antiquarks participate at leading order in the e^+p CC DIS reaction. Thus such interactions are a powerful tool for flavour-specific investigations of the parton distribution functions (PDFs). Since only left-handed quarks and right-handed antiquarks contribute to CC DIS, the distribution of the positron-quark centre-of-mass scattering angle, θ^* , is a sensitive probe of the chiral structure of the weak interaction.

Measurements of the CC DIS cross sections at HERA have been reported previously by the H1 [1–4] and ZEUS [5–7] collaborations. These data extended the kinematic region covered by fixed-target neutrino-nucleus scattering experiments [8–11] by about two orders of magnitude towards larger Q^2 , the negative square of the four-momentum transfer. In addition, the double-differential cross section, $d^2\sigma/dxdQ^2$, where x is the Bjorken scaling variable, was measured for the first time by the HERA collider experiments in e^+p scattering [7, 12] and more recently in e^-p scattering [13, 14].

This paper presents measurements of the e^+p CC DIS single-differential cross-sections $d\sigma/dQ^2$, $d\sigma/dx$ and $d\sigma/dy$, and of $d^2\sigma/dxdQ^2$. The results presented here are compared to the expectations of the SM. The measurements are based on 60.9 pb $^{-1}$ of data collected during the running periods in 1999 and 2000 when HERA collided 27.5 GeV positrons with 920 GeV protons, yielding a centre-of-mass energy (\sqrt{s}) of 318 GeV. The previous ZEUS measurement [7] at $\sqrt{s} = 300$ GeV was based on 47.7 pb $^{-1}$. Using the measured cross sections the mass of the W boson is determined and the helicity structure of the Standard Model is investigated. The structure-function F_2^{CC} is extracted for the first time at HERA and compared to a fixed-target result [15].

2 Standard Model prediction

The CC DIS differential cross section, $d^2\sigma_{\text{Born}}^{\text{CC}}/dxdQ^2$, for the reaction $e^+p \rightarrow \bar{\nu}_e X$ can be written at leading order in the electroweak interaction, for longitudinally unpolarised beams [16]:

$$\frac{d^2\sigma_{\text{Born}}^{\text{CC}}(e^+p)}{dxdQ^2} = \frac{G_{\text{F}}^2}{4\pi x} \frac{M_W^4}{(Q^2 + M_W^2)^2} \times [Y_+ F_{2,e^+p}^{\text{CC}}(x, Q^2) - y^2 F_{\text{L},e^+p}^{\text{CC}}(x, Q^2) - Y_- x F_{3,e^+p}^{\text{CC}}(x, Q^2)]. \quad (1)$$

In the equation, G_F is the Fermi constant, M_W is the mass of the W boson, x is the Bjorken scaling variable, $y = Q^2/xs$ (neglecting the masses of the incoming particles) and $Y_{\pm} = 1 \pm (1 - y)^2$. The centre-of-mass energy in the positron-proton collisions is given by $\sqrt{s} = 2\sqrt{E_e E_p}$, where E_e and E_p are the positron and proton beam energies, respectively. The inelasticity, y , is related to θ^* by $y = (1 - \cos\theta^*)/2$. The structure-functions $F_{2,e+p}^{CC}$ and $x F_{3,e+p}^{CC}$, at leading order in QCD, may be written in terms of sums and differences of quark and antiquark PDFs of the proton as follows:

$$F_{2,e+p}^{CC} = x[d(x, Q^2) + s(x, Q^2) + \bar{u}(x, Q^2) + \bar{c}(x, Q^2)], \quad (2)$$

$$x F_{3,e+p}^{CC} = x[d(x, Q^2) + s(x, Q^2) - \bar{u}(x, Q^2) - \bar{c}(x, Q^2)], \quad (3)$$

where, for example, the PDF $d(x, Q^2)$ gives the number density of down quarks with momentum fraction x at a given Q^2 . The longitudinal structure function, $F_{L,e+p}^{CC}$, is zero at leading order in QCD. At next-to-leading order (NLO) in QCD, $F_{L,e+p}^{CC}$ is non-zero but gives a negligible contribution to the cross section except at values of y close to 1, where the contribution can be as large as 10%. Since the top-quark mass is large and the off-diagonal elements of the CKM matrix are small [17], the contribution from third-generation quarks may be ignored in CC DIS at HERA [18]. All cross-section calculations presented in this paper were performed at NLO in the strong coupling constant.

3 The ZEUS experiment

A detailed description of the ZEUS detector can be found elsewhere [19]. A brief outline of the components most relevant for this analysis is given below.

Charged particles are tracked in the central tracking detector (CTD) [20], which operates in a magnetic field of 1.43 T provided by a thin superconducting solenoid. The CTD consists of 72 cylindrical drift chamber layers, organised in nine superlayers covering the polar-angle¹ region $15^\circ < \theta < 164^\circ$. The relative transverse-momentum resolution for full-length tracks is $\sigma(p_T)/p_T = 0.0058p_T \oplus 0.0065 \oplus 0.0014/p_T$, with p_T in GeV. The position of the interaction vertex along the beam direction can be reconstructed from the CTD tracks with a resolution of about 1 cm in CC events.

The high-resolution uranium-scintillator calorimeter (CAL) [21] consists of three parts: the forward (FCAL), the barrel (BCAL) and the rear (RCAL) calorimeter, covering 99.7%

¹ The ZEUS coordinate system is a right-handed Cartesian system, with the Z axis pointing in the proton beam direction, referred to as the “forward direction”, and the X axis pointing left towards the centre of HERA. The polar angle, θ , is measured with respect to the proton beam direction. The coordinate origin is at the nominal interaction point.

of the solid angle around the nominal interaction point. Each part is subdivided transversely into towers and longitudinally into one electromagnetic section (EMC) and either one (in RCAL) or two (in BCAL and FCAL) hadronic sections (HAC). The smallest subdivision of the calorimeter is called a cell. The CAL relative energy resolutions, as measured under test-beam conditions, are $\sigma(E)/E = 0.18/\sqrt{E}$ for electrons and $\sigma(E)/E = 0.35/\sqrt{E}$ for hadrons, with E in GeV. The timing resolution of the CAL is better than 1 ns for energy deposits exceeding 4.5 GeV. The position of the interaction vertex along the beam direction can be reconstructed from the arrival time of energy deposits in FCAL. The resolution is about 9 cm for events with FCAL energy above 25 GeV, improving to about 7 cm for FCAL energy above 100 GeV.

An instrumented-iron backing calorimeter (BAC) [22] surrounds the CAL and is used to measure energy leakage and to identify muons. Muon chambers in the forward, barrel and rear [23] regions are used in this analysis to veto background events induced by cosmic-ray or beam-halo muons.

The luminosity was measured using the Bethe-Heitler reaction $ep \rightarrow e\gamma p$. The photons were detected by the luminosity monitor [24], a lead-scintillator calorimeter placed in the HERA tunnel 107 m from the interaction point in the positron beam direction. The integrated luminosity used for this analysis was $60.9 \pm 1.4 \text{ pb}^{-1}$.

4 Monte Carlo simulation

Monte Carlo (MC) simulations were used to determine the efficiency for selecting events and the accuracy of kinematic reconstruction, to estimate the ep background rates and to extract cross sections for the full kinematic region. A sufficient number of events was generated to ensure that the statistical uncertainties arising from the MC simulation were negligible compared to those of the data. The MC samples were normalised to the total integrated luminosity of the data.

Charged current DIS events, including electroweak radiative effects, were simulated using the HERACLES 4.6.1 [25] program with the DJANGO 1.1 [26] interface to the MC generators that provide the hadronisation. Initial-state radiation, vertex and propagator corrections and two-boson exchange are included in HERACLES. The mass of the W boson was calculated using the PDG [17] values for the fine structure constant, the Fermi constant, the masses of the Z boson and the top quark, and with the Higgs-boson mass set to 100 GeV. The events were generated using the CTEQ5D [27] PDFs. The colour-dipole model of ARIADNE 4.10 [28] was used to simulate $\mathcal{O}(\alpha_S)$ plus leading logarithmic corrections to the result of the quark-parton model. As a systematic check, the MEPS

model of LEPTO 6.5 [29] was used. Both programs use the Lund string model of JETSET 7.4 [30] for the hadronisation. A set of NC events generated with DJANGO was used to estimate the NC contamination in the CC sample. Photoproduction background was estimated using events simulated with HERWIG 5.9 [31]. The background from W production was estimated using the EPVEC [32] generator, and the background from production of charged-lepton pairs was generated with the LPAIR [33] and GRAPE [34] programs.

The ZEUS detector response was simulated in detail with a program based on GEANT 3.13 [35]. The simulated events were subjected to the same trigger requirements as the data, and processed by the same reconstruction programs.

5 Reconstruction of kinematic variables

The principal signature of CC DIS at HERA is the presence of a large missing transverse momentum, $P_{T,\text{miss}}$, arising from the energetic final-state neutrino which escapes detection. The quantity $P_{T,\text{miss}}$ was calculated from

$$P_{T,\text{miss}}^2 = P_X^2 + P_Y^2 = \left(\sum_i E_i \sin \theta_i \cos \phi_i \right)^2 + \left(\sum_i E_i \sin \theta_i \sin \phi_i \right)^2,$$

where the sums run over all CAL energy deposits, E_i (uncorrected in the trigger, but corrected [36] for energy loss in inactive material and other effects in the offline analysis), and θ_i and ϕ_i are the polar and azimuthal angles of the calorimeter deposits as viewed from the interaction vertex. The polar angle of the hadronic system, γ_h , is defined by $\cos \gamma_h = (P_{T,\text{miss}}^2 - \delta^2)/(P_{T,\text{miss}}^2 + \delta^2)$, where $\delta = \sum_i E_i(1 - \cos \theta_i) = \sum_i (E - P_Z)_i$. In the naive quark-parton model, γ_h is the angle through which the struck quark is scattered. Finally, the total transverse energy, E_T , is given by $E_T = \sum_i E_i \sin \theta_i$.

The kinematic variables were reconstructed using the Jacquet-Blondel method [37]. The estimators of y , Q^2 and x are: $y_{\text{JB}} = \delta/(2E_e)$, $Q_{\text{JB}}^2 = P_{T,\text{miss}}^2/(1 - y_{\text{JB}})$, and $x_{\text{JB}} = Q_{\text{JB}}^2/(sy_{\text{JB}})$.

The resolution in Q^2 is about 20%. The resolution in x improves from about 20% at $x = 0.01$ to about 5% at $x = 0.5$. The resolution in y ranges from about 14% at $y = 0.05$ to about 8% at $y = 0.83$.

6 Event selection

Charged current DIS candidates were selected by requiring a large $P_{T,\text{miss}}$ and a reconstructed event vertex consistent with an ep interaction. The main sources of background

come from NC scattering and high- E_T photoproduction where the energy resolution of the CAL or energy that escapes detection can lead to significant measured missing transverse momentum. Non- ep events such as beam-gas interactions, beam-halo muons or cosmic rays can also cause substantial imbalance in the measured transverse momentum and constitute additional sources of background. The selection criteria described below were imposed to separate CC events from all backgrounds.

When the current jet lies in the central region of the detector, i.e. γ_h is large, tracks in the CTD can be used to reconstruct the event vertex, strongly suppressing non- ep backgrounds. For CC events with small γ_h , the charged particles of the hadronic final state are often outside the acceptance of the CTD. Such events populate the high- x region of the kinematic plane. The events were classified first according to γ_0 , the value of γ_h measured with respect to the nominal interaction point. Subsequently, the kinematic quantities were recalculated using the Z -coordinate of the event vertex (Z_{VTX}) determined from either CTD tracks, for events with large γ_0 , or the calorimeter-timing information for events in which γ_0 is small. The selection procedures for events with large and small γ_0 are described in Sections 6.2 and 6.3, respectively.

6.1 Trigger selection

ZEUS has a three-level trigger system [19, 38]. At the first level only coarse calorimeter and tracking information is available. Events were selected using criteria based on the energy, transverse energy and missing transverse momentum measured in the calorimeter. Generally, events were triggered with low thresholds on these quantities if a coincidence with CTD tracks from the event vertex occurred, while higher thresholds were required for events with no CTD tracks. Typical threshold values were 5 GeV (8 GeV) in missing transverse momentum, or 11.5 GeV (21 GeV) in transverse energy for events with (without) CTD tracks.

At the second level, timing information from the calorimeter was used to reject events inconsistent with the bunch-crossing time. In addition, the topology of the CAL energy deposits was used to reject background events. In particular, a tighter cut of 6 GeV (9 GeV for events without CTD tracks) was made on missing transverse momentum, since the resolution in this variable is better at the second level than at the first level.

At the third level, full track reconstruction and vertex finding were performed and used to reject candidate events with a vertex inconsistent with an ep interaction. Cuts were applied to calorimeter quantities and reconstructed tracks to further reduce beam-gas contamination.

The efficiency of the full trigger chain for CC DIS events, in the kinematic region of the cross section measurements, was determined using MC simulation to be 96%, and not below 78% in any cross-section bin.

6.2 Offline selection based on a CTD vertex

Events with $\gamma_0 > 0.4$ rad were required to have a vertex reconstructed from CTD tracks and to satisfy all of the following criteria.

- $|Z_{\text{VTX}}| < 50$ cm: the primary vertex reconstructed from the CTD tracks was required to be within the range consistent with the ep interaction region. The X - and Y -vertex positions were set to zero since the CTD vertex resolution in X and Y is larger than the displacement of the beam line from the origin.
- $P_{T,\text{miss}} > 12$ GeV and $P'_{T,\text{miss}} > 10$ GeV: $P'_{T,\text{miss}}$ is the missing transverse momentum calculated excluding the FCAL towers closest to the beam hole. The $P'_{T,\text{miss}}$ cut strongly suppresses beam-gas events while maintaining high efficiency for CC events.
- Tracking requirement: tracks associated with the event vertex with transverse momentum in excess of 0.2 GeV and a polar angle in the range 15° to 164° were defined as “good” tracks. In order to remove beam-gas background at least one such tracks was required and a cut was also applied in two dimensions on the number of good tracks versus the total number of tracks.
- Rejection of photoproduction: $P_{T,\text{miss}}/E_T > 0.4$ was required for events with $P_{T,\text{miss}} < 30$ GeV. This cut was raised to $P_{T,\text{miss}}/E_T > 0.55$ for events with $P_{T,\text{miss}} < 20$ GeV. This selected events with a collimated energy flow, as expected from a single scattered quark.

For events with $P_{T,\text{miss}} < 20$ GeV, the number of good tracks within an azimuthal angle of 0.5 rad around the direction of the $P_{T,\text{miss}}$ was counted (N_+) as well as the number of tracks opposite to the $P_{T,\text{miss}}$ direction (N_-). The event was rejected if the number of tracks in the $P_{T,\text{miss}}$ direction was ≥ 2 , or if the asymmetry defined as $(N_- - N_+)/ (N_- + N_+)$ was less than 0.7.

For charged current events there is a correlation between the direction of the $P_{T,\text{miss}}$ vector calculated using CTD tracks and that obtained using the CAL. The difference between these quantities was required to be less than 0.5 radians for $P_{T,\text{miss}} < 20$ GeV and less than 2.0 radians for $P_{T,\text{miss}} \geq 20$ GeV.

- Rejection of NC DIS: NC DIS events in which the scattered positron or jet energies are poorly measured can have a considerable apparent missing transverse momentum. To identify such events, a search for candidate positrons was made using isolated

electromagnetic clusters in the CAL [39] for events with $P_{T,\text{miss}} < 30$ GeV. Candidate positron clusters within the CTD acceptance were required to have an energy above 4 GeV and a matching track with momentum larger than 25% of the cluster energy. Clusters with $\theta > 164^\circ$ were required to have a transverse momentum exceeding 2 GeV. Events with a candidate positron satisfying the above criteria and $\delta > 30$ GeV were rejected, since for fully contained NC events, δ peaks at $2E_e = 55$ GeV.

- Rejection of non- ep background: Muon-finding algorithms [40] based on CAL energy deposits or muon-chamber signals were used to reject events produced by cosmic rays or muons in the beam halo.

All events were visually inspected, and 5 cosmic-ray and halo-muon events were removed. A total of 1164 data events satisfied these criteria, in good agreement with 1183 predicted by the MC simulation.

6.3 Offline selection based on a CAL vertex

For events with $\gamma_0 < 0.4$ rad, the following criteria were imposed.

- $|Z_{\text{VTX}}| < 50$ cm: Z_{VTX} was reconstructed from the measured arrival time of energy deposits in FCAL [41]. The X - and Y -vertex positions were set to zero.
- $P_{T,\text{miss}} > 14$ GeV and $P'_{T,\text{miss}} > 12$ GeV: the conditions on missing transverse momentum were tightened, compensating for the relaxation of the requirements on tracks.
- Rejection of non- ep background: the muon-rejection cuts described in Section 6.2 were used. A class of background events arose from beam-halo muons that produced a shower inside the FCAL. To reduce this background, topological cuts on the transverse and longitudinal shower shape were imposed; these cuts rejected events in which the energy deposits were more collimated than for typical hadronic jets.

All events were visually inspected, and 11 cosmic-ray and halo-muon events were removed. A total of 292 data events satisfied these criteria, in good agreement with 285 predicted by the MC simulation.

6.4 Final event sample

To restrict the sample to kinematic regions where the resolution in the kinematic variables was good and the backgrounds small, the requirements $Q_{\text{JB}}^2 > 200$ GeV² and $y_{\text{JB}} < 0.9$ were imposed.

Figure 1 compares the distributions of data events entering the final CC sample with the MC expectation for the sum of the CC signal and ep background events. The MC simulations give a good description of the data.

7 Cross-section determination and systematic uncertainties

The cross sections were determined using bin-by-bin unfolding. The measured cross section in a particular kinematic bin, for example for $d^2\sigma/dxdQ^2$, was determined from

$$\frac{d^2\sigma}{dxdQ^2} = \frac{N_{\text{data}} - N_{\text{bg}}}{N_{\text{MC}}} \cdot \frac{d^2\sigma_{\text{Born}}^{\text{SM}}}{dxdQ^2},$$

where N_{data} is the number of data events, N_{bg} is the number of background events expected from MC, N_{MC} is the number of signal MC events expected and $\frac{d^2\sigma_{\text{Born}}^{\text{SM}}}{dxdQ^2}$ is the Standard Model prediction evaluated using the on-shell scheme [17]. A similar procedure was used for $d\sigma/dQ^2$, $d\sigma/dx$ and $d\sigma/dy$. Consequently, the acceptance, bin-centring and radiative corrections were all taken from the MC simulation. The cross-sections $d\sigma/dQ^2$ and $d\sigma/dx$ were extrapolated to the full y range using the SM predictions with CTEQ5D PDFs. The extrapolation factors ranged from 3% at the lowest Q^2 to 28% at the highest Q^2 in $d\sigma/dQ^2$ and from zero to 8% in $d\sigma/dx$.

The systematic uncertainties in the measured cross sections were determined by changing the selection cuts or the analysis procedure in turn and repeating the extraction of the cross sections. The following systematic studies were carried out.

- Uncertainty of the calorimeter energy scale: the relative uncertainty of the hadronic energy scale was determined to be 2% for the RCAL and 1% for the FCAL and BCAL [14]. Varying the energy scale of the calorimeter sections by these amounts in the detector simulation induces small shifts of the Jacquet-Blondel estimators for the kinematic variables.

The variation of the energy scale of each of the calorimeters simultaneously up or down by these amounts gave the systematic uncertainty on the total measured energy in the calorimeter. This was found to give shifts in the cross sections which were correlated between kinematic bins (δ_1 in Tables 1 and 2).

By increasing (decreasing) the FCAL and RCAL energy scales together while the BCAL energy scale was decreased (increased) the uncertainty in the cross sections from the effect of the energy scale on the measurement of γ_h was obtained. This was

also found to give shifts in the cross sections which were correlated between kinematic bins (δ_2 in Tables 1 and 2).

The sensitivity of the cross section measurements to the fractions of the energy deposited in the EMC and HAC sections of the calorimeter was determined by simultaneously increasing the energy measured in the EMC section of the calorimeter by 2% and decreasing the energy measured in the HAC section by 2%, and vice-versa. This was done separately for each of the calorimeter sections.

The final systematic error attributed to the uncertainty in the hadronic energy scale was obtained by taking the quadratic sum of these three types of estimate. The resulting systematic shifts in the measured cross sections were typically within $\pm 5\%$, but increase to $\pm 20\%$ in the highest Q^2 and x bins.

- Energy leakage: 4% of the accepted events have a measurable energy leakage from the CAL into the BAC. The average leakage of transverse energy for these events is 5% of that observed in the CAL. Both the fraction of events with leakage and the average amount of leakage are well modelled by the MC simulation and the effect on the cross-section measurement is negligible.
- Variation of selection thresholds: the selection thresholds were varied by the typical resolution of the CAL quantities ($\pm 10\%$) in both data and MC and no significant systematic effects were observed. The criteria for good tracks was also varied and no systematic effects in the measured cross sections were observed.
- Uncertainty in the parton-shower scheme: the MEPS model of LEPTO was used instead of the ARIADNE model. This gave shifts in the cross sections which were found to be correlated between kinematic bins (δ_3 in Tables 1 and 2). The largest effects were observed in the bins at high Q^2 ($\pm 20\%$) and highest and lowest x ($\pm 6\%$). The largest effect in the double-differential cross section was seen in the low- Q^2 , low- x bins, where it amounted to $\pm 10\%$.
- Background subtraction: the uncertainty in the small contribution from photoproduction background was estimated by fitting a linear combination of the $P_{T,\text{miss}}/E_T$ distributions of the signal and the background MC samples to the corresponding distribution in the data, allowing the normalisation (N_{PhP}) of the photoproduction MC events to vary. No cut on $P_{T,\text{miss}}/E_T$ was applied for this check. Varying N_{PhP} by $\pm 20\%$, corresponding to twice the uncertainty given by the fit, results in modifications of the cross sections within $\pm 2\%$.
- Choice of parton distribution functions: the CC MC events were generated using the CTEQ5D PDFs [27]. The ZEUS-S fit [42] was used to examine the influence of variations of the PDFs on the cross-section measurement through differences in the acceptance and bin-centring corrections. Monte Carlo events were re-weighted to the

extremes of the cross-section prediction allowed by the fit. The change in the measured cross section was typically $< 1\%$, except at high Q^2 where it was -5% and at high x where it was $+4\%$.

- The effect of NLO QCD corrections: the DJANGO program neglects the F_L contribution and NLO QCD corrections to xF_3 when generating CC events. The corresponding effect on the cross-section measurement was evaluated by re-weighting the MC events with the ratio of the cross sections with and without NLO QCD corrections. The largest effect, of -3% , was observed in the highest y bin.

The individual uncertainties were added in quadrature separately for the positive and negative deviations from the nominal cross-section values to obtain the total systematic uncertainties listed in Tables 1 and 2. The $\mathcal{O}(\alpha)$ electroweak corrections to CC DIS have been discussed by several authors [43, 44]. Various theoretical approximations and computer codes gave differences in the CC cross sections of typically $\pm(1 - 2)\%$ or less. However, the differences can be as large as $\pm(3 - 8)\%$ at high x and high y . This uncertainty and the uncertainty of 2.25% on the measured total luminosity were not included in the total systematic uncertainty.

8 Results

The total cross section for e^+p CC DIS in the kinematic region $Q^2 > 200 \text{ GeV}^2$ is

$$\sigma_{\text{tot}}^{\text{CC}}(Q^2 > 200 \text{ GeV}^2) = 34.8 \pm 0.9(\text{stat.})_{-1.0}^{+0.9}(\text{syst.}) \text{ pb.}$$

In this case the uncertainty in the measured luminosity was included in the systematic uncertainty. The result is in agreement with the SM expectation of $37.0_{-0.8}^{+1.7}$ pb evaluated using the ZEUS-S fit.

8.1 Single-differential cross sections

The single-differential cross-sections $d\sigma/dQ^2$, $d\sigma/dx$ and $d\sigma/dy$ for $Q^2 > 200 \text{ GeV}^2$ are shown in Figs. 2, 3 and 4, respectively, and compiled in Table 1 including details of the systematic uncertainties that are correlated between cross-section bins. The SM cross sections derived from Eq. (1) using the ZEUS-S fit, the CTEQ6D [45] and the MRST(2001) [46] parameterisations of the PDFs are shown, together with the ratios of the measured cross sections to the SM cross section evaluated with the ZEUS-S fit.

The cross sections $d\sigma/dQ^2$ and $d\sigma/dx$ both drop by four orders of magnitude due to the effect of the W -boson propagator and the decreasing quark density at large x . The

ZEUS-S fit was based on fixed-target DIS data obtained at much lower Q^2 ($< 100 \text{ GeV}^2$) and from ZEUS NC data at large Q^2 . The excellent description of the data by the SM prediction based on this fit confirms both the decomposition of the proton momentum into different quark flavours, specifically the down quark contribution, and the evolution of parton distributions towards scales considerably larger than the W -boson mass. At very large x and Q^2 , the uncertainty in the prediction derived from the ZEUS-S fit, and also the global fits, reflects the lack of data constraining the d -quark density.

8.2 Double-differential cross sections

The reduced double-differential cross section, $\tilde{\sigma}$, is defined by

$$\tilde{\sigma} = \left[\frac{G_F^2}{2\pi x} \left(\frac{M_W^2}{M_W^2 + Q^2} \right)^2 \right]^{-1} \frac{d^2\sigma}{dx dQ^2}.$$

At leading order in QCD, $\tilde{\sigma}(e^+p \rightarrow \bar{\nu}_e X)$ depends on the quark momentum distributions as follows:

$$\tilde{\sigma}(e^+p \rightarrow \bar{\nu}_e X) = x [\bar{u} + \bar{c} + (1-y)^2(d+s)]. \quad (4)$$

The reduced cross sections are displayed as functions of Q^2 and x in Figs. 5 and 6, respectively, and compiled in Table 2 including details of the systematic uncertainties that are correlated between cross-section bins. The predictions of Eq. (1), evaluated using the ZEUS-S fit, the CTEQ6D and the MRST(2001) PDFs give a good description of the data. The contributions from the PDF combinations $(d+s)$ and $(\bar{u} + \bar{c})$, obtained in the $\overline{\text{MS}}$ scheme from the ZEUS-S fit, are shown separately in Fig. 6.

8.3 Helicity studies

The W boson couples only to left-handed fermions and right-handed antifermions. Therefore, the angular distribution of the scattered quark in $e^+\bar{q}$ CC DIS will be flat in θ^* , while it will exhibit a $(1 + \cos\theta^*)^2$ distribution in e^+q scattering. Since $(1-y)^2 \propto (1 + \cos\theta^*)^2$, the helicity structure of CC interactions can be illustrated by plotting the reduced double-differential cross section of Eq. (4) versus $(1-y)^2$ in bins of x . In the region of approximate scaling, i.e. $x \sim 0.1$, this yields a straight line. At leading order in QCD the intercept of this line gives the $(\bar{u} + \bar{c})$ contribution, while the slope gives the $(d+s)$ contribution.

Figure 7 shows $\tilde{\sigma}$ as a function of $(1-y)^2$ for the e^+p CC DIS data, compared to the previously published e^-p data [14]. At large x , e^+p CC DIS is sensitive to the valence part

of $d(x, Q^2)$ while e^-p CC DIS is sensitive to the valence part of $u(x, Q^2)$. Equivalently to Eq. (4), the reduced cross section for e^-p CC DIS can be written as

$$\tilde{\sigma}(e^-p \rightarrow \nu_e X) = x [u + c + (1 - y)^2(\bar{d} + \bar{s})],$$

permitting a similar interpretation for the intercept and slope in terms of the appropriate parton densities. Scaling violations can be observed in the theoretical prediction as $(1 - y)^2$ approaches 1. The data agree with the expectation of the SM from the ZEUS-S fit.

8.4 Mass of the W boson

The fall in the cross-section $d\sigma/dQ^2$ with increasing Q^2 depends on $M_W^4/(Q^2 + M_W^2)^2$. Fitting $d\sigma/dQ^2$ with G_F fixed at the PDG [17] value of $1.16639 \cdot 10^{-5} \text{ GeV}^{-2}$, using the ZEUS-S fit PDFs and M_W treated as a free parameter gives:

$$M_W = 78.9 \pm 2.0(\text{stat.}) \pm 1.8(\text{syst.})_{-1.8}^{+2.0}(\text{PDF}) \text{ GeV},$$

where the third uncertainty was estimated by varying the PDFs within the uncertainties given by the ZEUS-S fit. The systematic uncertainty includes contributions from the sources identified in Section 7 and the uncertainty on the measured luminosity. This measurement, in the space-like region, is in good agreement with the more precise measurements of W -boson mass in the time-like region [17].

8.5 Extraction of F_2^{CC}

It is possible to extract the quark singlet distribution, F_2^{CC} , for the first time at HERA by combining the measurements presented in this paper with the previous ZEUS e^-p CC DIS results [14]. This can be compared to the corresponding result from fixed-target neutrino-nucleon scattering. Equations 2 and 3 show that only down-type quarks and up-type antiquarks contribute to e^-p CC DIS in the Standard Model. The cross section for e^-p CC DIS is given by

$$\frac{d^2\sigma_{\text{Born}}^{\text{CC}}(e^-p)}{dx dQ^2} = \frac{G_F^2}{4\pi x} \frac{M_W^4}{(Q^2 + M_W^2)^2} [Y_+ F_{2,e^-p}^{\text{CC}}(x, Q^2) - y^2 F_{L,e^-p}^{\text{CC}}(x, Q^2) + Y_- x F_{3,e^-p}^{\text{CC}}(x, Q^2)],$$

where the structure-functions F_{2,e^-p}^{CC} and $x F_{3,e^-p}^{\text{CC}}$, at leading order in QCD, may be written in terms of sums and differences of quark and antiquark PDFs:

$$F_{2,e^-p}^{\text{CC}} = x[u(x, Q^2) + c(x, Q^2) + \bar{d}(x, Q^2) + \bar{s}(x, Q^2)],$$

$$x F_{3,e^-p}^{\text{CC}} = x[u(x, Q^2) + c(x, Q^2) - \bar{d}(x, Q^2) - \bar{s}(x, Q^2)].$$

Therefore, the sum of F_{2,e^+p}^{CC} and F_{2,e^-p}^{CC} represents the contribution from all quark and antiquark flavours and can be extracted from the measured CC cross sections as

$$F_2^{\text{CC}} = \frac{4\pi x}{G_F^2} \left(\frac{M_W^2 + Q^2}{M_W^2} \right)^2 \frac{1}{Y_+} \left(\frac{d^2\sigma_{\text{Born}}^{\text{CC}}(e^+p)}{dx dQ^2} + \frac{d^2\sigma_{\text{Born}}^{\text{CC}}(e^-p)}{dx dQ^2} \right) + \Delta(xF_3, F_L),$$

where $\Delta(xF_3, F_L)$ denotes a correction term taking into account the xF_3 and F_L structure functions. The correction is given by

$$\Delta(xF_3, F_L) = \frac{Y_-}{Y_+} \left(xF_{3,e^+p}^{\text{CC}} - xF_{3,e^-p}^{\text{CC}} \right) + \frac{y^2}{Y_+} \left(F_{L,e^+p}^{\text{CC}} + F_{L,e^-p}^{\text{CC}} \right).$$

The dominant uncertainty on the extracted structure function is statistical. The systematic uncertainties δ_1 , δ_2 , δ_3 (defined in Section 7) and the luminosity uncertainties were considered fully correlated between the two data sets. The other systematic uncertainties were treated as uncorrelated. Figure 8 shows the extracted structure-function F_2^{CC} as a function of Q^2 , for different values of x . The size of the correction $\Delta(xF_3, F_L)$, computed at NLO in QCD using the ZEUS-S fit, is shown as a shaded area in each bin. It can be seen that the correction term is smaller than the uncertainties on the measurement for low values of x but becomes sizeable at higher values of x and Q^2 . The uncertainty on the correction $\Delta(xF_3, F_L)$ was also computed using the ZEUS-S fit and found to be small. The corresponding result for νFe interactions from the CCFR Collaboration [15] is shown, after correcting for heavy-target effects [47]. It can be seen that both sets of results, spanning more than four orders of magnitude in Q^2 , are well described by the SM prediction evaluated using the ZEUS-S fit. Note that the CCFR F_2^{CC} results were not included in the ZEUS-S fit.

9 Summary

Differential cross sections for charged current deep inelastic scattering, $e^+p \rightarrow \bar{\nu}_e X$, have been measured for $Q^2 > 200 \text{ GeV}^2$ using 60.9 pb^{-1} of data collected with the ZEUS detector during the period 1999 to 2000. The double-differential cross-section $d^2\sigma/dx dQ^2$ has been measured in the kinematic range $280 \text{ GeV}^2 < Q^2 < 17\,000 \text{ GeV}^2$ and $0.008 < x < 0.42$. The chiral structure of the Standard Model was investigated by plotting the double-differential cross section as a function of $(1-y)^2$. The mass of the W boson, determined from a fit to $d\sigma/dQ^2$, is $M_W = 78.9 \pm 2.0 \text{ (stat.)} \pm 1.8 \text{ (syst.)} {}_{-1.8}^{+2.0} \text{ (PDF) GeV}$. The singlet structure-function F_2^{CC} has been extracted for the first time at HERA, by combining the measurements presented here with previous ZEUS measurements. The Standard Model gives an excellent description of all the data confirming the decomposition of the proton momentum into different quark flavours, specifically the down-quark

distribution, and also verifies the QCD evolution of parton distributions towards scales considerably larger than the W -boson mass.

Acknowledgements

We appreciate the contributions to the construction and maintenance of the ZEUS detector of the many people who are not listed as authors. The HERA machine group and the DESY computing staff are especially acknowledged for their success in providing excellent operation of the collider and the data-analysis environment. We thank the DESY directorate for their strong support and encouragement.

References

- [1] H1 Coll., T. Ahmed et al., Phys. Lett. **B 324**, 241 (1994).
- [2] H1 Coll., S. Aid et al., Z. Phys. **C 67**, 565 (1995).
- [3] H1 Coll., S. Aid et al., Phys. Lett. **B 379**, 319 (1996).
- [4] H1 Coll., C. Adloff et al., Preprint DESY-03-038 (hep-ex/0304003), 2003. Submitted to Eur. Phys. J.
- [5] ZEUS Coll., M. Derrick et al., Phys. Rev. Lett. **75**, 1006 (1995).
- [6] ZEUS Coll., M. Derrick et al., Z. Phys. **C 72**, 47 (1996).
- [7] ZEUS Coll., J. Breitweg et al., Eur. Phys. J. **C 12**, 411 (2000). Erratum in Eur. Phys. J. **C 27**, 305 (2003).
- [8] CDHS Coll., H. Abramowicz et al., Z. Phys. **C 25**, 29 (1984).
- [9] CDHSW Coll., J.P. Berge et al., Z. Phys. **C 49**, 187 (1991).
- [10] CCFR Coll., E. Oltman et al., Z. Phys. **C 53**, 51 (1992).
- [11] BEBC Coll., G.T. Jones et al., Z. Phys. **C 62**, 575 (1994).
- [12] H1 Coll., C. Adloff et al., Eur. Phys. J. **C 13**, 609 (2000).
- [13] H1 Coll., C. Adloff et al., Eur. Phys. J. **C 19**, 269 (2001).
- [14] ZEUS Coll., S. Chekanov et al., Phys. Lett. **B 539**, 197 (2002). Erratum in Phys. Lett. **B 552**, 308 (2003).
- [15] CCFR/NuTeV Coll., U.K. Yang et al., Phys. Rev. Lett. **86**, 2742 (2001).
- [16] A.M. Cooper-Sarkar, R.C.E. Devenish and A. De Roeck, Int. J. Mod. Phys. **A 13**, 3385 (1998).
- [17] Particle Data Group, D.E. Groom et al., Eur. Phys. J. **C 15**, 1 (2000).
- [18] U.F. Katz, *Deep-Inelastic Positron-Proton Scattering in the High-Momentum-Transfer Regime of HERA*, Springer Tracts in Modern Physics, Vol. 168. Springer, Berlin, Heidelberg, 2000.
- [19] ZEUS Coll., U. Holm (ed.), *The ZEUS Detector*. Status Report (unpublished), DESY (1993), available on <http://www-zeus.desy.de/bluebook/bluebook.html>.
- [20] N. Harnew et al., Nucl. Inst. Meth. **A 279**, 290 (1989);
B. Foster et al., Nucl. Phys. Proc. Suppl. **B 32**, 181 (1993);
B. Foster et al., Nucl. Inst. Meth. **A 338**, 254 (1994).

- [21] M. Derrick et al., Nucl. Inst. Meth. **A 309**, 77 (1991);
A. Andresen et al., Nucl. Inst. Meth. **A 309**, 101 (1991);
A. Caldwell et al., Nucl. Inst. Meth. **A 321**, 356 (1992);
A. Bernstein et al., Nucl. Inst. Meth. **A 336**, 23 (1993).
- [22] H. Abramowicz et al., Nucl. Inst. Meth. **A 313**, 126 (1992).
- [23] G. Abbiendi et al., Nucl. Inst. Meth. **A 333**, 342 (1993).
- [24] J. Andruszków et al., Preprint DESY-92-066, DESY, 1992;
ZEUS Coll., M. Derrick et al., Z. Phys. **C 63**, 391 (1994);
J. Andruszków et al., Acta Phys. Pol. **B 32**, 2025 (2001).
- [25] A. Kwiatkowski, H. Spiesberger and H.-J. Möhring, Comp. Phys. Comm. **69**, 155 (1992). Also in *Proc. Workshop Physics at HERA*, 1991, DESY, Hamburg;
H. Spiesberger, *An Event Generator for ep Interactions at HERA Including Radiative Processes (Version 4.6)*, 1996, available on
<http://www.desy.de/~hspiesb/heracles.html>.
- [26] H. Spiesberger, *HERACLES and DJANGO: Event Generation for ep Interactions at HERA Including Radiative Processes*, 1998, available on
<http://www.desy.de/~hspiesb/djangoh.html>.
- [27] CTEQ Coll., H.L. Lai et al., Eur. Phys. J. **C 12**, 375 (2000).
- [28] L. Lönnblad, Comp. Phys. Comm. **71**, 15 (1992).
- [29] G. Ingelman, A. Edin and J. Rathsman, Comp. Phys. Comm. **101**, 108 (1997).
- [30] T. Sjöstrand, Comp. Phys. Comm. **39**, 347 (1986);
T. Sjöstrand and M. Bengtsson, Comp. Phys. Comm. **43**, 367 (1987);
T. Sjöstrand, Comp. Phys. Comm. **82**, 74 (1994).
- [31] G. Marchesini et al., Comp. Phys. Comm. **67**, 465 (1992).
- [32] U. Baur, J.A.M. Vermaseren and D. Zeppenfeld, Nucl. Phys. **B 375**, 3 (1992).
- [33] S.P. Baranov et al., *Proc. Workshop on Physics at HERA*, W. Buchmüller and G. Ingelman (eds.), Vol. 3, p. 1478. DESY, Hamburg, Germany (1991).
- [34] T. Abe, Comp. Phys. Comm. **136**, 126 (2001).
- [35] R. Brun et al., GEANT3, Technical Report CERN-DD/EE/84-1, CERN, 1987.
- [36] ZEUS Coll., J. Breitweg et al., Eur. Phys. J. **C 11**, 427 (1999).
- [37] F. Jacquet and A. Blondel, *Proceedings of the Study for an ep Facility for Europe*, U. Amaldi (ed.), p. 391. Hamburg, Germany (1979). Also in preprint DESY 79/48.

- [38] W.H. Smith, K. Tokushuku and L.W. Wiggers, *Proc. Computing in High-Energy Physics (CHEP)*, Annecy, France, Sept. 1992, C. Verkerk and W. Wojcik (eds.), p. 222, CERN, Geneva, Switzerland (1992). Also in preprint DESY 92-150B.
- [39] H. Abramowicz, A. Caldwell and R. Sinkus, *Nucl. Inst. Meth.* **A 365**, 508 (1995); R. Sinkus and T. Voss, *Nucl. Inst. Meth.* **A 391**, 360 (1997).
- [40] A. Kruse. Ph.D. Thesis, Amsterdam University, 1999.
- [41] ZEUS Coll., M. Derrick et al., *Phys. Lett.* **B 316**, 412 (1993).
- [42] ZEUS Coll., S. Chekanov et al., *Phys. Rev.* **D 67**, 012007 (2003).
- [43] A.M. Cooper-Sarkar et al., *J. Phys.* **G 25**, 1387 (1999).
- [44] B. Heinemann, S. Riess and H. Spiesberger, *Proc. Workshop on Monte Carlo Generators for HERA Physics*, G. Grindhammer et al. (ed.), p. 530. DESY, Hamburg, Germany (1999). Also in preprint DESY-PROC-1999-02, available on <http://www.desy.de/~heramc/>.
- [45] J. Pumplin et al., *JHEP* **07**, 012 (2002).
- [46] A.D. Martin et al., *Eur. Phys. J.* **C23**, 73 (2002).
- [47] A.D. Martin et al., *Nucl. Phys. Proc. Suppl.* **B 79**, 105 (1999). *Proc. 7th Int. Workshop on Deep Inelastic Scattering and QCD (DIS99)*, J. Blümlein and T. Riemann (eds.). Zeuthen, Germany, April 1999.

$d\sigma/dQ^2$								
Q^2 range (GeV ²)	Q^2 (GeV ²)	N_{data}	N_{bg}	$\delta_{\text{unc}}(\%)$	$\delta_1(\%)$	$\delta_2(\%)$	$\delta_3(\%)$	$d\sigma/dQ^2$ (pb/GeV ²)
200 - 400	280	159	14.2	+2.0 -3.1	+1.9 -1.8	+0.1 -0.5	± 3.8	$(2.85 \pm 0.22^{+0.13}_{-0.15}) \cdot 10^{-2}$
400 - 711	530	204	2.3	+1.8 -1.5	+1.7 -0.8	+0.8 +0.8	± 1.6	$(1.81 \pm 0.13^{+0.06}_{-0.04}) \cdot 10^{-2}$
711 - 1265	950	306	4.2	+1.0 -1.2	+0.7 -1.0	-0.5 -0.5	± 2.7	$(1.30 \pm 0.08^{+0.04}_{-0.04}) \cdot 10^{-2}$
1265 - 2249	1700	324	1.4	+1.2 -0.9	+0.5 -0.0	+0.3 +0.2	± 1.6	$(7.16 \pm 0.41^{+0.15}_{-0.13}) \cdot 10^{-3}$
2249 - 4000	3000	235	0.9	+1.1 -1.0	-1.9 +1.8	-0.1 +0.2	± 0.6	$(2.90 \pm 0.19^{+0.06}_{-0.07}) \cdot 10^{-3}$
4000 - 7113	5300	155	0.2	+0.8 -1.1	-2.2 +2.9	+0.1 +0.6	± 0.4	$(1.07 \pm 0.09^{+0.03}_{-0.03}) \cdot 10^{-3}$
7113 - 12649	9500	59	0.2	+1.8 -1.1	+0.3 -6.4	+0.3 -1.9	± 2.6	$(2.20 \pm 0.29^{+0.15}_{-0.16}) \cdot 10^{-4}$
12649 - 22494	17000	11	0.0	+1.5 -2.7	-8.8 +11	+2.5 -2.4	± 6.5	$(2.05^{+0.82}_{-0.61} \pm 0.26_{-0.23}) \cdot 10^{-5}$
22494 - 60000	30000	3	0.0	+4.7 -6.3	-16 +18	+5.1 -7.8	± 21	$(2.12^{+2.06}_{-1.15} \pm 0.60_{-0.59}) \cdot 10^{-6}$
$d\sigma/dx$								
x range	x	N_{data}	N_{bg}	$\delta_{\text{unc}}(\%)$	$\delta_1(\%)$	$\delta_2(\%)$	$\delta_3(\%)$	$d\sigma/dx$ (pb)
0.010 - 0.022	0.015	167	7.7	+1.0 -1.3	+2.2 -0.9	+0.1 -0.0	± 5.5	$(4.58 \pm 0.36^{+0.28}_{-0.26}) \cdot 10^2$
0.022 - 0.046	0.032	351	6.2	+0.5 -0.7	+0.4 -0.4	+0.1 +0.2	± 0.9	$(2.92 \pm 0.16^{+0.03}_{-0.04}) \cdot 10^2$
0.046 - 0.100	0.068	425	4.8	+0.6 -0.9	-0.5 +0.6	+0.7 -0.6	± 0.3	$(1.59 \pm 0.08^{+0.02}_{-0.02}) \cdot 10^2$
0.100 - 0.178	0.130	258	0.9	+0.6 -0.6	-0.8 +1.0	+0.9 -0.6	± 0.9	$(7.22 \pm 0.45^{+0.13}_{-0.11}) \cdot 10^1$
0.178 - 0.316	0.240	173	0.5	+0.8 -0.5	-2.2 +2.4	-1.3 +1.3	± 0.7	$(3.01 \pm 0.23^{+0.09}_{-0.08}) \cdot 10^1$
0.316 - 0.562	0.420	45	0.1	+1.1 -0.8	-4.3 +4.1	-3.2 +3.1	± 3.7	$(5.98 \pm 0.90^{+0.38}_{-0.39}) \cdot 10^0$
0.562 - 1.000	0.650	2	0.0	+6.5 -2.1	-12 +14	-11 +16	± 8.7	$(4.43^{+5.84}_{-2.87} \pm 1.06_{-0.81}) \cdot 10^{-1}$
$d\sigma/dy$								
y range	y	N_{data}	N_{bg}	$\delta_{\text{unc}}(\%)$	$\delta_1(\%)$	$\delta_2(\%)$	$\delta_3(\%)$	$d\sigma/dy$ (pb)
0.00 - 0.10	0.05	264	7.0	+0.8 -1.2	+0.5 -0.6	+0.2 -0.1	± 1.7	$(7.79 \pm 0.48^{+0.15}_{-0.17}) \cdot 10^1$
0.10 - 0.20	0.15	360	6.3	+0.5 -0.8	+0.4 -0.2	-0.3 +0.4	± 1.0	$(6.86 \pm 0.37^{+0.08}_{-0.09}) \cdot 10^1$
0.20 - 0.34	0.27	316	4.1	+0.5 -0.8	-0.3 +0.2	-0.8 +0.7	± 3.5	$(4.46 \pm 0.25^{+0.16}_{-0.16}) \cdot 10^1$
0.34 - 0.48	0.41	219	1.9	+0.7 -0.6	-0.0 +0.5	-0.1 +0.5	± 0.2	$(3.36 \pm 0.23^{+0.03}_{-0.02}) \cdot 10^1$
0.48 - 0.62	0.55	146	2.3	+1.0 -1.0	-0.2 +0.7	+1.0 -0.5	± 2.2	$(2.58 \pm 0.21^{+0.07}_{-0.06}) \cdot 10^1$
0.62 - 0.76	0.69	102	1.4	+1.5 -1.5	-2.3 +3.1	+2.6 -2.5	± 1.8	$(2.15 \pm 0.22^{+0.10}_{-0.09}) \cdot 10^1$
0.76 - 0.90	0.83	49	0.4	+3.0 -3.0	-4.2 +4.3	+2.9 -2.4	± 1.8	$(1.53 \pm 0.22^{+0.10}_{-0.09}) \cdot 10^1$

Table 1: Values of the differential cross-sections $d\sigma/dQ^2$, $d\sigma/dx$ and $d\sigma/dy$. The following quantities are given: the kinematic range of the measurement; the value of x, y and Q^2 at which the cross section is quoted; the number of data events; the number of expected background events; the uncorrelated systematic uncertainty; those systematic uncertainties with correlations between cross-section bins δ_1 , δ_2 and δ_3 defined in Section 7 and the measured cross section, with statistical and total systematic uncertainties. The uncertainty on the measured luminosity of 2.25% is not included in the total systematic uncertainty.

Q^2 (GeV ²)	x	N_{data}	N_{bg}	$\delta_{\text{unc}}(\%)$	$\delta_1(\%)$	$\delta_2(\%)$	$\delta_3(\%)$	$\bar{\sigma}$
280	0.008	26	2.5	+2.8 -2.8	+4.4 -2.5	+0.3 +2.1	± 5.3	$(1.47 \pm 0.28^{+0.11}_{-0.09}) \cdot 10^0$
280	0.015	49	5.3	+1.9 -3.0	+1.4 -2.2	-0.6 -0.1	± 10	$(1.08 \pm 0.15^{+0.11}_{-0.12}) \cdot 10^0$
280	0.032	55	3.3	+1.5 -1.9	+2.1 +0.2	+1.6 -0.6	± 3.1	$(8.52 \pm 1.12^{+0.37}_{-0.31}) \cdot 10^{-1}$
280	0.068	24	2.8	+0.8 -5.1	+0.6 -4.0	-0.7 -1.7	± 1.0	$(4.14 \pm 0.78^{+0.06}_{-0.28}) \cdot 10^{-1}$
530	0.015	52	0.5	+1.0 -1.0	+2.1 -0.7	-0.9 +0.3	± 7.6	$(8.39 \pm 1.18^{+0.67}_{-0.65}) \cdot 10^{-1}$
530	0.032	57	0.7	+1.0 -0.8	+0.5 -1.3	-0.2 +0.9	± 3.7	$(6.15 \pm 0.82^{+0.24}_{-0.25}) \cdot 10^{-1}$
530	0.068	59	0.6	+1.8 -1.3	+1.6 +0.5	+2.1 +0.9	± 2.4	$(6.28 \pm 0.83^{+0.26}_{-0.17}) \cdot 10^{-1}$
530	0.130	25	0.2	+7.2 -1.1	+4.2 +1.2	+4.1 +2.5	± 10	$(4.40 \pm 0.89^{+0.61}_{-0.44}) \cdot 10^{-1}$
950	0.015	52	2.0	+2.0 -1.6	+1.1 +0.6	+1.5 -0.9	± 8.5	$(6.85 \pm 0.94^{+0.61}_{-0.59}) \cdot 10^{-1}$
950	0.032	102	0.8	+0.5 -0.6	+1.5 -0.7	-0.4 +0.5	± 5.4	$(6.97 \pm 0.70^{+0.40}_{-0.39}) \cdot 10^{-1}$
950	0.068	84	0.8	+0.5 -1.6	-0.4 -0.9	-1.0 -0.2	± 2.0	$(5.63 \pm 0.62^{+0.11}_{-0.16}) \cdot 10^{-1}$
950	0.130	48	0.2	+0.5 -4.0	+0.6 -3.8	-0.4 -2.7	± 1.4	$(4.86 \pm 0.71^{+0.08}_{-0.31}) \cdot 10^{-1}$
950	0.240	20	0.3	+5.1 -1.1	+0.9 -0.7	-4.5 -0.4	± 4.4	$(2.87 \pm 0.64^{+0.20}_{-0.19}) \cdot 10^{-1}$
1700	0.032	105	0.9	+0.9 -0.8	-1.0 -0.6	+0.4 -0.0	± 3.2	$(5.55 \pm 0.55^{+0.19}_{-0.19}) \cdot 10^{-1}$
1700	0.068	105	0.2	+1.2 -0.5	+1.1 +0.4	-0.1 +0.5	± 1.0	$(4.84 \pm 0.48^{+0.10}_{-0.05}) \cdot 10^{-1}$
1700	0.130	57	0.2	+1.3 -0.6	+0.4 +0.9	+1.5 -0.2	± 3.3	$(3.71 \pm 0.50^{+0.15}_{-0.13}) \cdot 10^{-1}$
1700	0.240	39	0.1	+1.3 -3.4	-0.4 +0.4	-0.5 +0.2	± 3.6	$(2.73 \pm 0.44^{+0.10}_{-0.14}) \cdot 10^{-1}$
3000	0.068	97	0.3	+0.9 -1.6	-2.2 +2.2	+2.1 -1.3	± 1.1	$(3.71 \pm 0.39^{+0.13}_{-0.12}) \cdot 10^{-1}$
3000	0.130	55	0.1	+1.0 -0.5	-2.0 +1.6	-1.4 +1.9	± 3.2	$(2.73 \pm 0.37^{+0.12}_{-0.11}) \cdot 10^{-1}$
3000	0.240	44	0.1	+2.3 -0.5	-2.1 +2.1	-1.3 +1.8	± 3.0	$(2.17 \pm 0.33^{+0.10}_{-0.08}) \cdot 10^{-1}$
3000	0.420	7	0.0	+3.5 -1.3	-0.4 +1.4	-2.3 +1.7	± 3.1	$(4.24^{+2.29}_{-1.57} \pm 0.22^{+0.22}_{-0.17}) \cdot 10^{-2}$
5300	0.068	49	0.1	+1.0 -1.4	-2.7 +2.3	+1.3 -2.5	± 2.3	$(2.28 \pm 0.33^{+0.08}_{-0.10}) \cdot 10^{-1}$
5300	0.130	45	0.0	+0.8 -0.8	-1.4 +2.5	+1.0 +0.1	± 1.2	$(1.96 \pm 0.29^{+0.06}_{-0.04}) \cdot 10^{-1}$
5300	0.240	41	0.0	+0.9 -0.7	-2.4 +3.7	-2.0 +4.4	± 0.7	$(1.80 \pm 0.28^{+0.11}_{-0.06}) \cdot 10^{-1}$
5300	0.420	20	0.0	+1.1 -3.9	-2.7 +3.8	-2.4 +4.2	± 3.6	$(9.85 \pm 2.22^{+0.67}_{-0.63}) \cdot 10^{-2}$
9500	0.130	21	0.1	+3.5 -2.4	-6.7 +5.8	+5.2 -5.7	± 3.9	$(9.99 \pm 2.18^{+0.94}_{-0.99}) \cdot 10^{-2}$
9500	0.240	22	0.0	+1.0 -2.2	-4.2 +3.6	-3.5 +1.3	± 3.6	$(1.03 \pm 0.22^{+0.06}_{-0.07}) \cdot 10^{-1}$
9500	0.420	8	0.0	+3.4 -0.6	-7.6 +6.1	-6.2 +5.7	± 0.3	$(3.78^{+1.86}_{-1.31} \pm 0.34^{+0.34}_{-0.37}) \cdot 10^{-2}$
17000	0.240	3	0.0	+3.9 -2.8	-8.8 +11	+6.1 -5.0	± 6.5	$(1.55^{+1.49}_{-0.84} \pm 0.23^{+0.23}_{-0.19}) \cdot 10^{-2}$
17000	0.420	6	0.0	+0.7 -3.8	-7.0 +7.8	-6.5 +5.6	± 2.8	$(3.19^{+1.91}_{-1.27} \pm 0.32^{+0.32}_{-0.34}) \cdot 10^{-2}$

Table 2: Values of the reduced cross section. The following quantities are given: the values of Q^2 and x at which the cross section is quoted; the number of data events; the number of expected background events; the uncorrelated systematic uncertainty; those systematic uncertainties with correlations between cross-section bins δ_1 , δ_2 and δ_3 defined in Section 7 and the measured cross section, with statistical and total systematic uncertainties. The uncertainty on the measured luminosity of 2.25% is not included in the total systematic uncertainty.

ZEUS

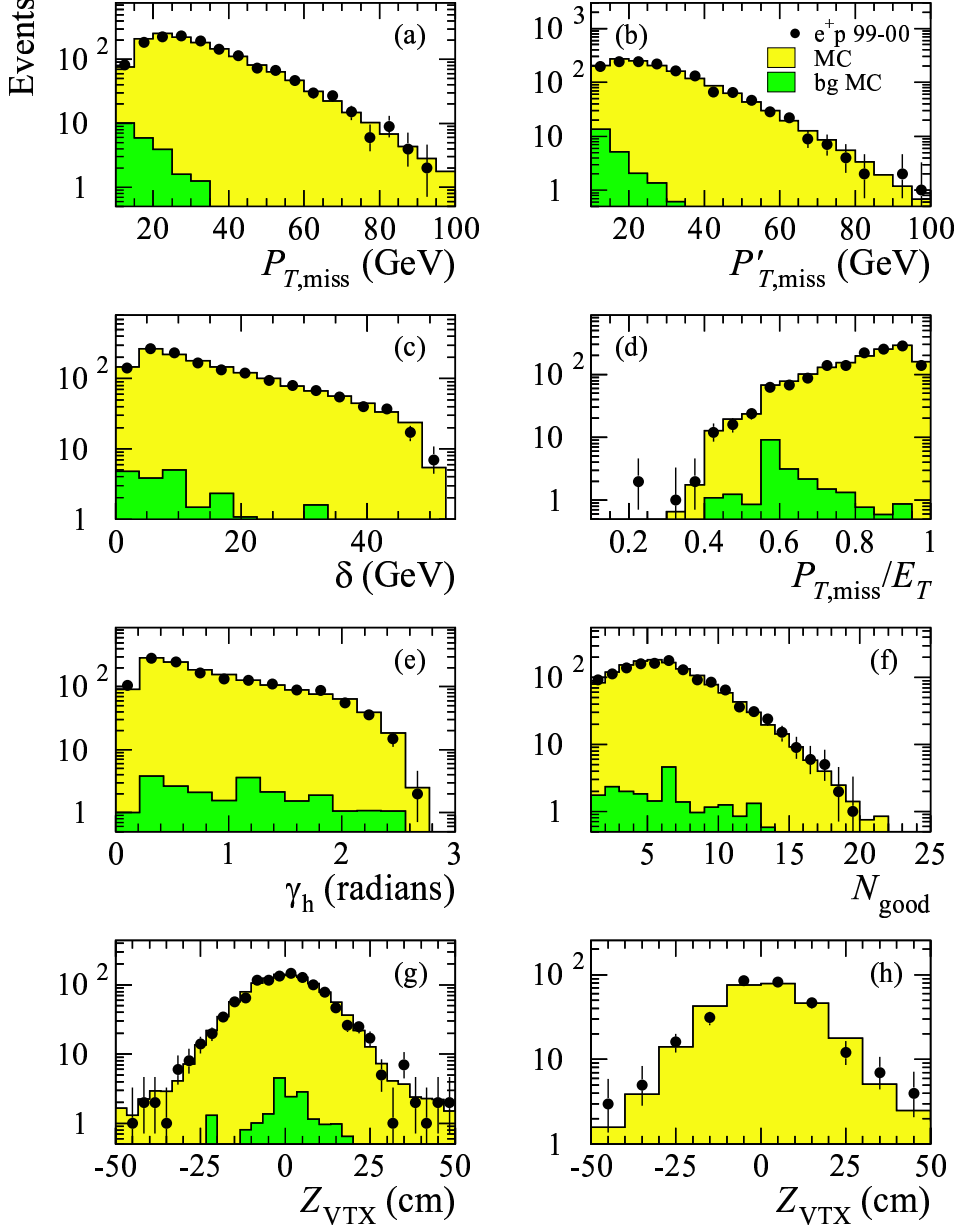


Figure 1: Comparison of the final e^+p CC data sample (solid points) with the sums of the signal and ep background Monte Carlo simulations (light shaded histograms). The ep background simulated events are shown as the dark shaded histograms. Shown are the distributions of (a) the missing transverse momentum, $P_{T,miss}$, (b) $P_{T,miss}$ excluding the very forward cells, $P'_{T,miss}$, (c) the variable δ , defined in Section 5, (d) the ratio of missing transverse momentum to total transverse energy, $P_{T,miss}/E_T$, (e) γ_h , (f) the number of good tracks, (g) the Z position of the CTD vertex for the high- γ_0 sample and (h) the Z position of the timing vertex for the low- γ_0 sample.

ZEUS

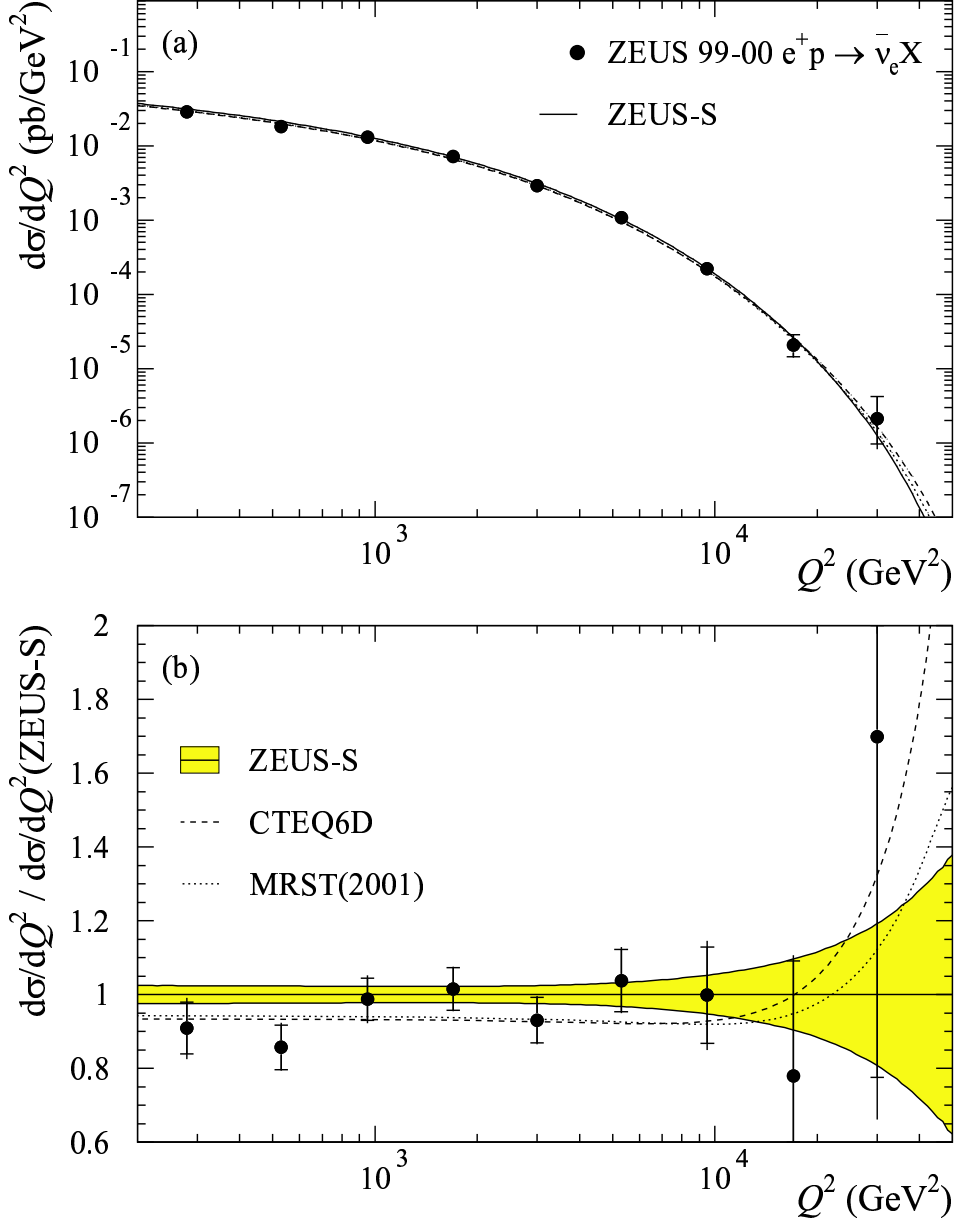


Figure 2: (a) The e^+p CC DIS Born cross-section $d\sigma/dQ^2$ for data and the Standard Model expectation evaluated using the ZEUS-S, the CTEQ6D and the MRST (2001) PDFs. The data are shown as the filled points, the statistical uncertainties are indicated by the inner error bars (delimited by horizontal lines) and the full error bars show the total uncertainty obtained by adding the statistical and systematic contributions in quadrature. (b) The ratio of the measured cross section, $d\sigma/dQ^2$, to the Standard Model expectation evaluated using the ZEUS-S fit. The shaded band shows the uncertainties from the ZEUS-S fit.

ZEUS

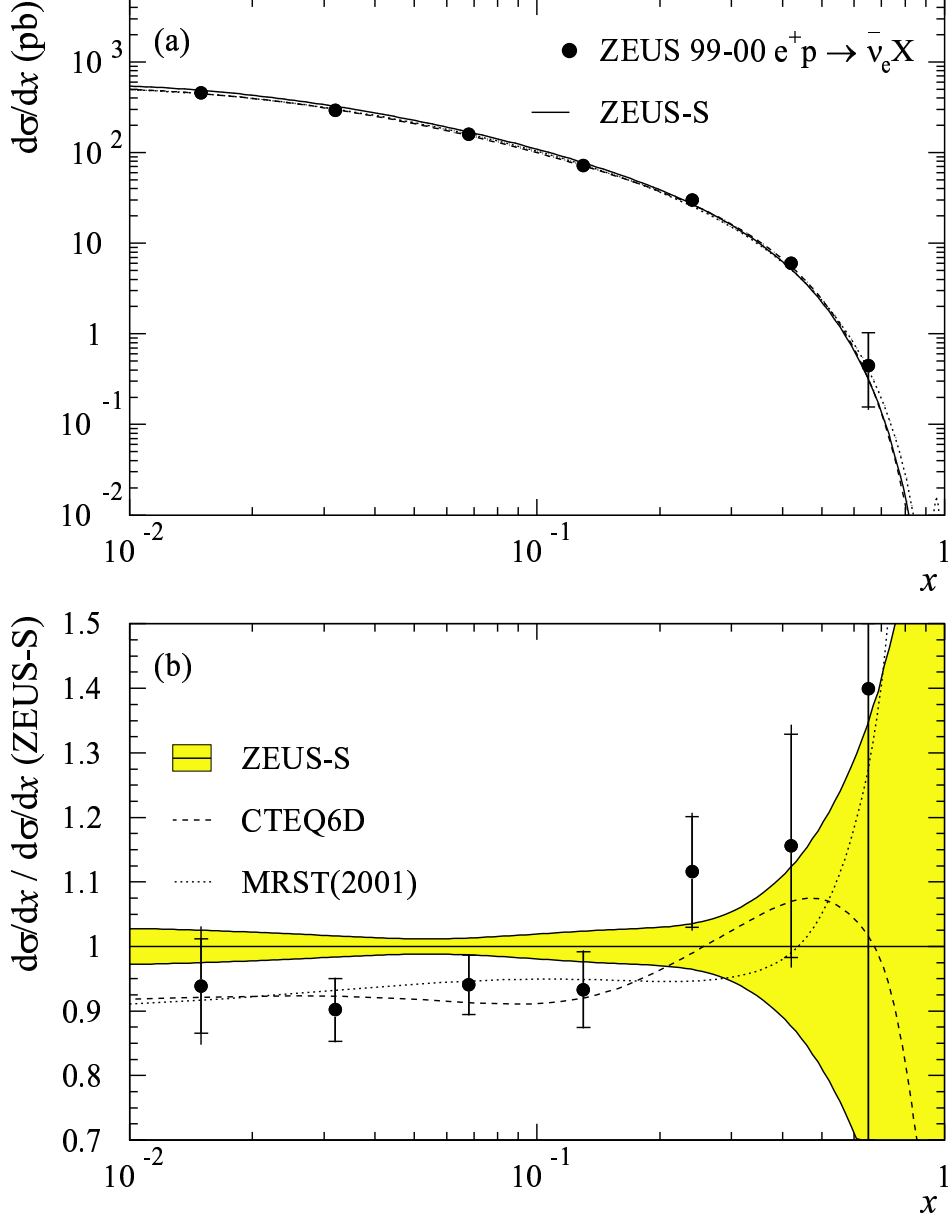


Figure 3: (a) The e^+p CC DIS Born cross-section $d\sigma/dx$ for data and the Standard Model expectation evaluated using the ZEUS-S, the CTEQ6D and the MRST (2001) PDFs. The data are shown as the filled points, the statistical uncertainties are indicated by the inner error bars (delimited by horizontal lines) and the full error bars show the total uncertainty obtained by adding the statistical and systematic contributions in quadrature. (b) The ratio of the measured cross section, $d\sigma/dx$, to the Standard Model expectation evaluated using the ZEUS-S fit. The shaded band shows the uncertainties from the ZEUS-S fit.

ZEUS

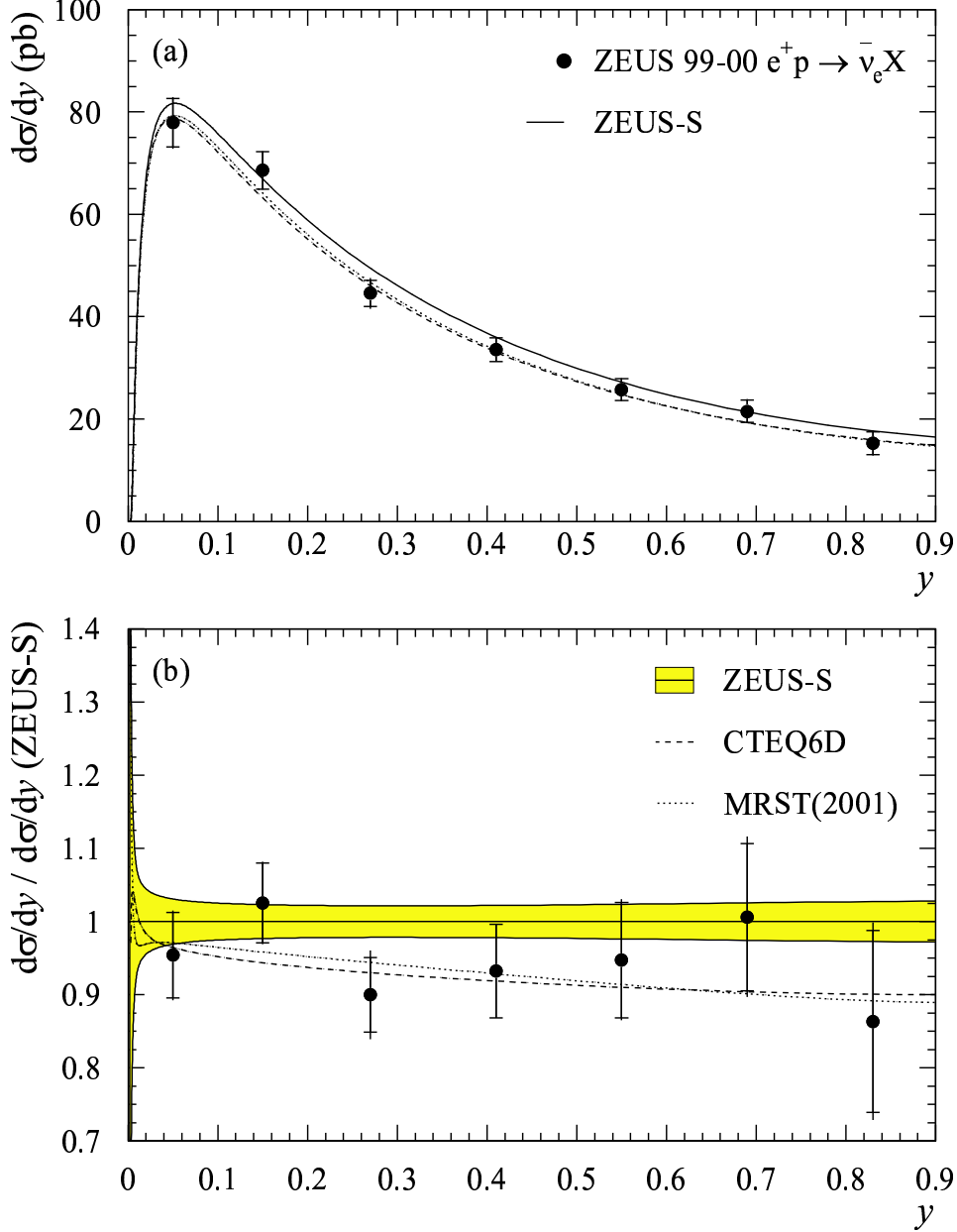


Figure 4: (a) The e^+p CC DIS Born cross-section $d\sigma/dy$ for data and the Standard Model expectation evaluated using the ZEUS-S, the CTEQ6D and the MRST (2001) PDFs. The data are shown as the filled points, the statistical uncertainties are indicated by the inner error bars (delimited by horizontal lines) and the full error bars show the total uncertainty obtained by adding the statistical and systematic contributions in quadrature. (b) The ratio of the measured cross section, $d\sigma/dy$, to the Standard Model expectation evaluated using the ZEUS-S fit. The shaded band shows the uncertainties from the ZEUS-S fit.

ZEUS

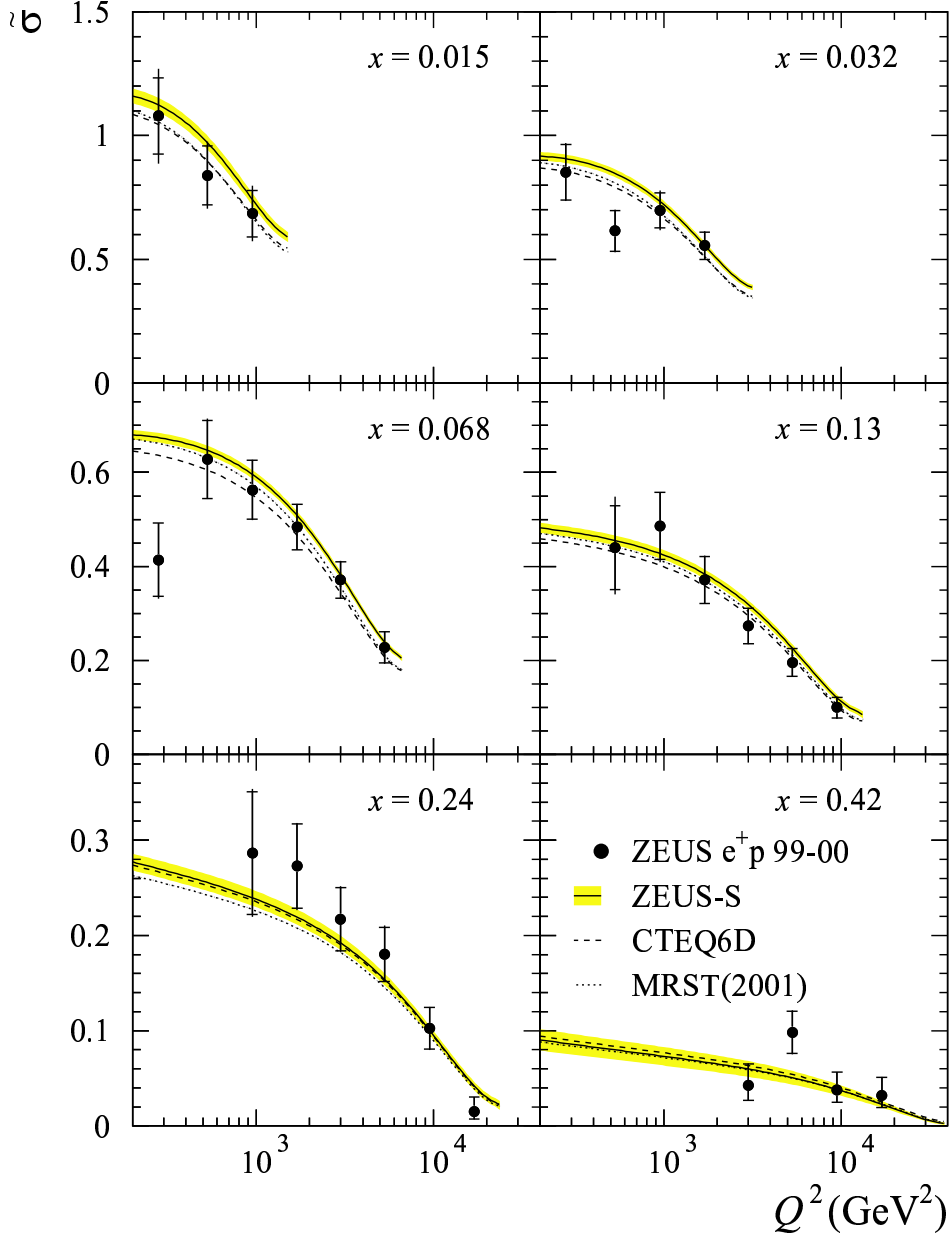


Figure 5: The reduced cross section, $\tilde{\sigma}$, as a function of Q^2 , for different fixed values of x . The data are shown as the filled points, the statistical uncertainties are indicated by the inner error bars (delimited by horizontal lines) and the full error bars show the total uncertainty obtained by adding the statistical and systematic contributions in quadrature. The expectation of the Standard Model evaluated using the ZEUS-S, the CTEQ6D and the MRST(2001) PDFs is shown by the solid, dashed and dotted lines, respectively. The shaded band shows the uncertainties from the ZEUS-S fit.

ZEUS

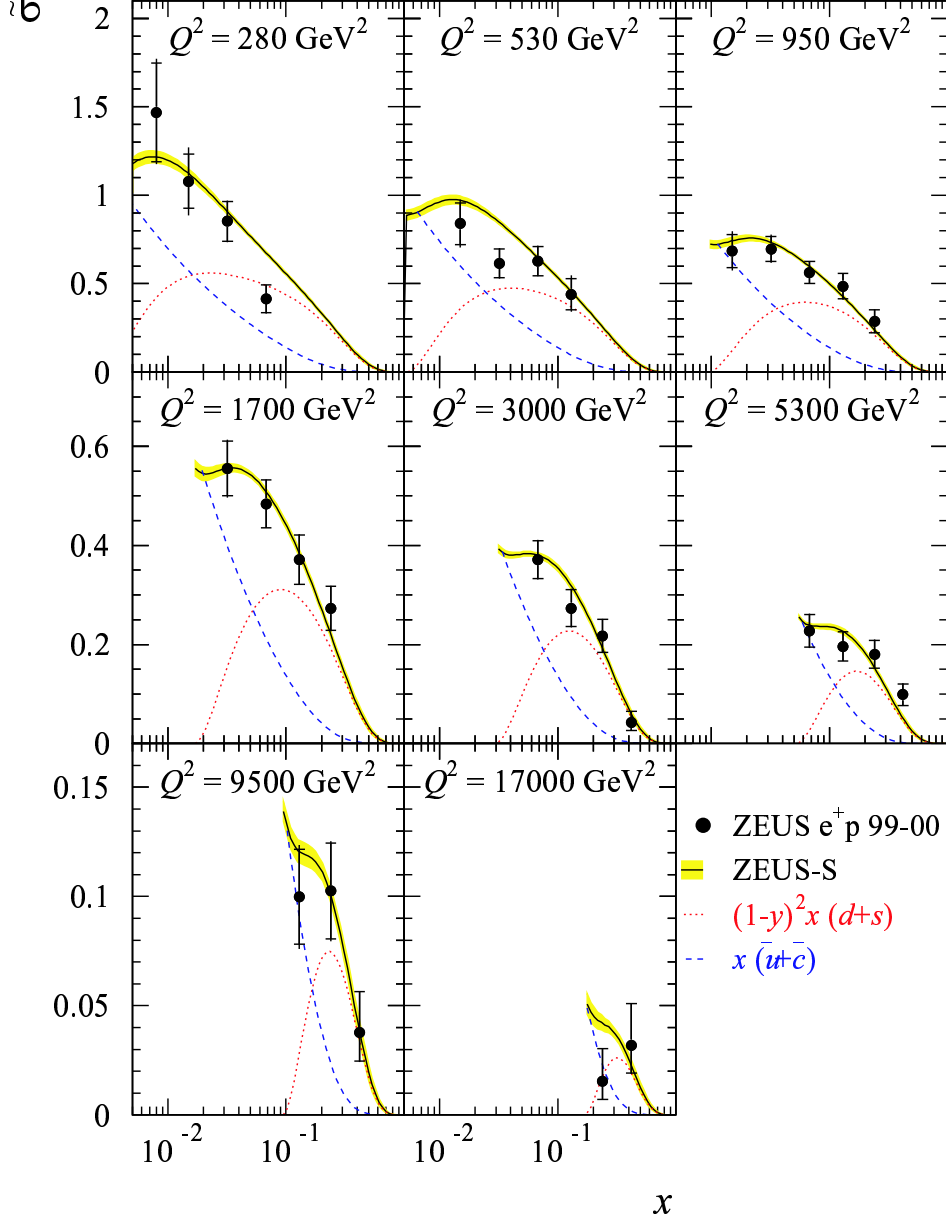


Figure 6: The reduced cross section, $\tilde{\sigma}$, as a function of x , for different values of Q^2 . The data are shown as the filled points, the statistical uncertainties are indicated by the inner error bars (delimited by horizontal lines) and the full error bars show the total uncertainty obtained by adding the statistical and systematic contributions in quadrature. The expectation of the Standard Model evaluated using the ZEUS-S fit is shown as a solid line. The shaded band shows the uncertainties from the ZEUS-S fit. The separate contributions of the PDF combinations $x(\bar{u} + \bar{c})$ and $(1-y)^2 x(d+s)$ are shown by the dotted and dashed lines, respectively.

ZEUS

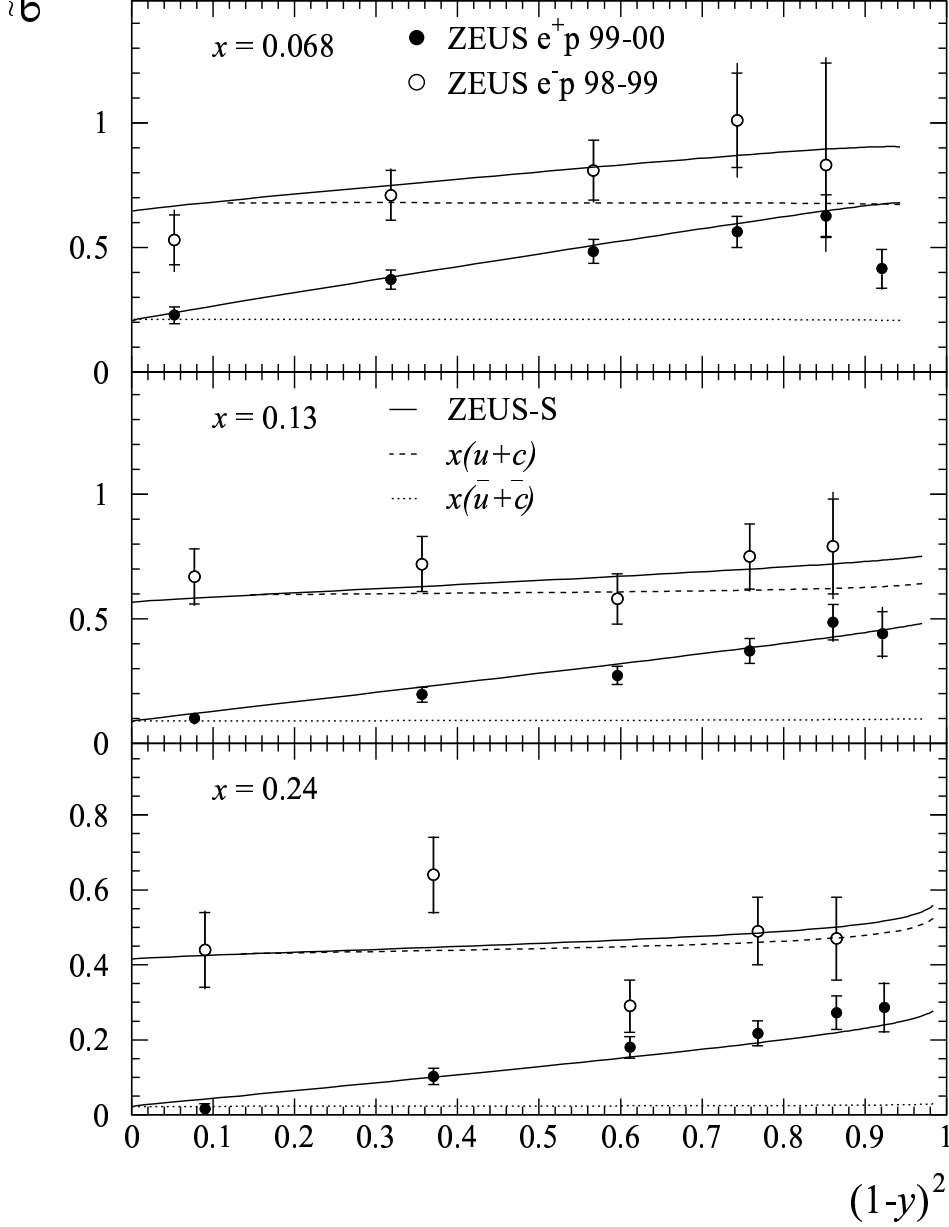


Figure 7: The reduced cross section, $\tilde{\sigma}$, as a function of $(1-y)^2$, for different fixed values of x , for e^+p (solid points) and e^-p (open circles) CC DIS. The data are shown as the points, the statistical uncertainties are indicated by the inner error bars (delimited by horizontal lines) and the full error bars show the total uncertainty obtained by adding the statistical and systematic contributions in quadrature. The expectation of the Standard Model evaluated using the ZEUS-S fit is shown as a solid line. The contributions of the PDF combinations $x(u+c)$ and $x(\bar{u}+\bar{c})$ are shown by the dashed and dotted lines, respectively.

ZEUS

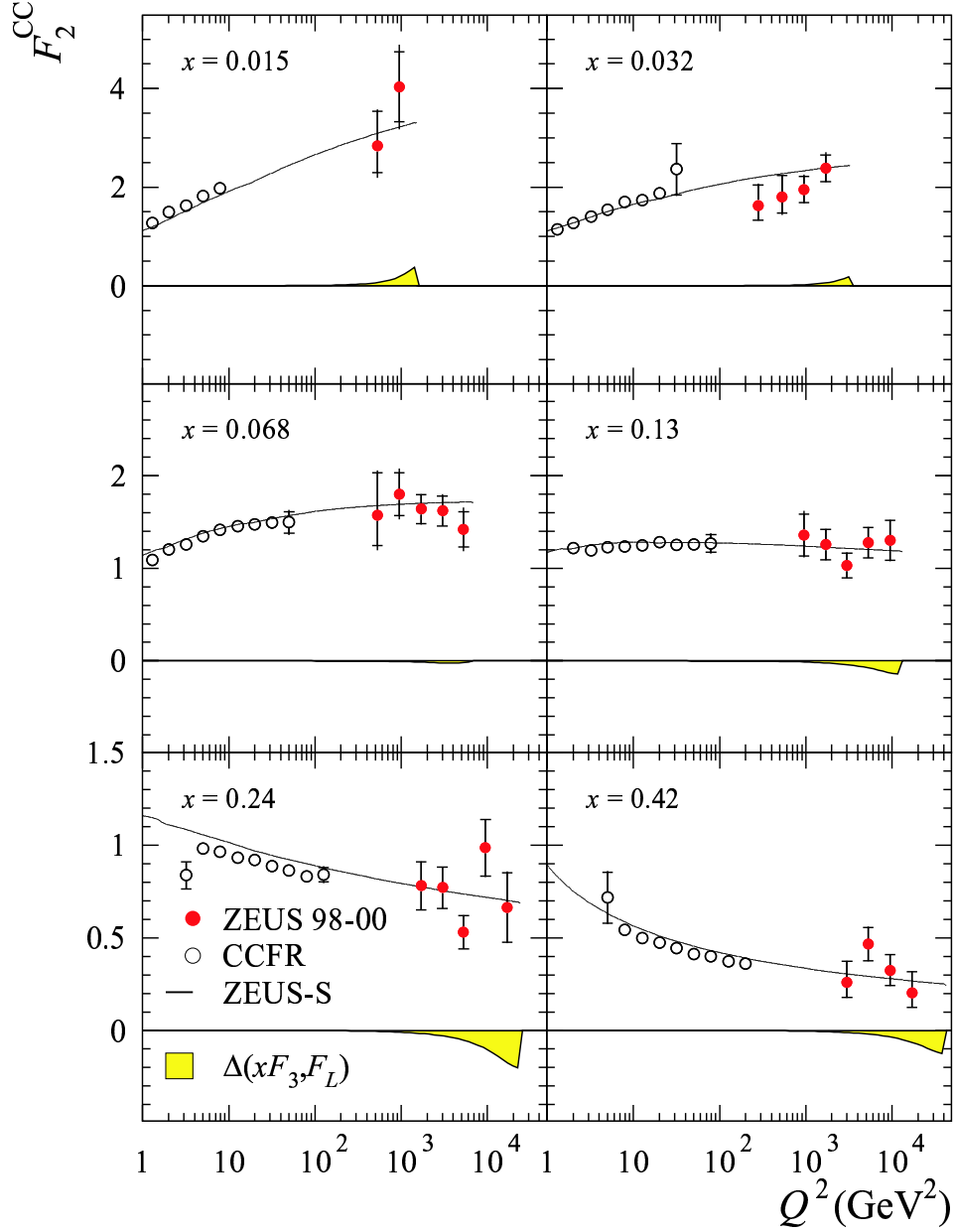


Figure 8: The structure function F_2^{CC} as a function of Q^2 , for different fixed values of x , extracted from ZEUS data (solid points) and compared to CCFR measurements corrected for heavy-target effects (open circles). The expectation of the Standard Model evaluated using the ZEUS-S fit is shown as a solid line. The shaded band shows the size of the correction $\Delta(xF_3, F_L)$ defined in Section 8.5.